

# Curvature Invariants for Lorentzian Traversable Wormholes

B. Mattingly<sup>1,2†</sup>, A. Kar<sup>1,2</sup>, M. D. Ali<sup>1,2</sup>, A. Baas<sup>1,2</sup>, C. Elmore<sup>1,2</sup>, C. Watson<sup>1,2</sup>,  
B. Shakerin<sup>1,2</sup>, E. W. Davis<sup>1,3</sup> and G. B. Cleaver<sup>1,2</sup>

<sup>1</sup>*Early Universe, Cosmology and Strings (EUCOS) Group, Center for Astrophysics, Space Physics and Engineering Research (CASPER), Baylor University, Waco, TX 76798, USA*

<sup>2</sup>*Department of Physics, Baylor University, Waco, TX 76798, USA*

<sup>3</sup>*Institute for Advanced Studies at Austin, 11855 Research Blvd., Austin, TX 78759, USA*

**Abstract:** A process for using curvature invariants is applied as a new means to evaluate the traversability of Lorentzian wormholes. This approach was formulated by Henry, Overduin and Wilcomb for Black Holes in Reference [1]. Curvature invariants are independent of coordinate basis, so the process is free of coordinate mapping distortions. The fourteen G'eh'eniau and Debever (GD) invariants are calculated and the non-zero, independent curvature invariant functions are plotted. Three example traversable wormhole metrics (*i*) thin-shell flat-face, (*ii*) spherically symmetric Morris and Thorne, and (*iii*) thin-shell Schwarzschild wormholes are investigated and are demonstrated to be traversable.

**Keywords:** Traversable Wormhole, Curvature Invariant, General Relativity.

**PACS:** 04.20.-q, 04.20.Cv, 02.40.-k.

## 1 Introduction

Lorentzian traversable wormholes were first predicted by Kip Thorne and collaborators who used Einstein's general relativistic field equations to explore the possibility of Faster-Than-Light (FTL) interstellar spaceflight without violating Special Relativity [2, 3]. References [4, 5] published earlier studies that demonstrated the possibility of traversable

---

<sup>†</sup>mailto: [Brandon.Mattingly@Baylor.edu](mailto:Brandon.Mattingly@Baylor.edu)

wormholes in general relativity. A Lorentzian traversable wormhole is a topological opening in spacetime which manifests traversable intra-universe and/or inter-universe connections, as well as different chronological connections between distant spacetime points. The Lorentzian traversable wormhole is free of both event horizons and singularities. It is fully traversable in both directions, geodesically complete, and there are no crushing gravitational tidal forces found anywhere inside the wormhole. Consequently, Lorentzian traversable wormholes are unlike the non-traversable Schwarzschild wormhole, or Einstein-Rosen bridge, associated with eternal black holes in the maximally extended version of the Schwarzschild metric. Unfortunately, exotic matter, which violates the point-wise and averaged energy conditions, is required to open and stabilize a Lorentzian traversable wormhole. A comprehensive technical overview of this subject is found in [6].

Studies of Lorentzian traversable wormholes rely on calculating the elements of the Riemann curvature tensor,  $R^i{}_{jkl}$ , to “observe” the effects of the wormhole’s spacetime curvature on photons and matter moving through it. However, the  $R^i{}_{jkl}$  cannot be calculated in an invariant manner (being functions of the chosen coordinates). Thus, analysis of  $R^i{}_{jkl}$  can be misleading because coordinate mapping distortions may arise as an artifact of the coordinate choice. The only way to properly illustrate wormhole spacetimes without such issues is to plot their independent curvature invariants and provide proper visualization of any hidden surprises.

Christoffel proved that scalars constructed from the metric and its derivatives must be functions of the metric itself and the Riemann tensor and its covariant derivatives [7]. Curvature invariants are scalar products of Riemann, Ricci or Weyl tensors, or their covariant derivatives. To visualize curved spacetime phenomena without distortion is to plot only the curvature invariants – quantities whose value are the same regardless of the choice of coordinates.

Fourteen curvature invariants have been defined in the literature but the total rises to seventeen when certain non-degenerate cases are taken into account [8]. Henry et al. [1] conducted a study which computed and plotted a number of independent curvature invariants for the hidden interiors of Kerr-Newman black holes. They produced visually stunning 3D plots which revealed the surprisingly complex nature of spacetime curvature in Kerr-Newman black hole interiors. This work motivated the present authors to undertake a similar study for the case of Lorentzian traversable wormholes. Reported here are the computations and 3D plots for three selected Lorentzian traversable wormholes that are described in [6]: (i) the thin-shell flat-face (TS) wormhole, (ii) the Morris and Thorne (MT) wormhole, and (iii) the thin-shell Schwarzschild wormhole.

## 2 Method to Compute the Invariants

To find the invariants, the following are required: metric  $g_{ij}$ , affine connection  $\Gamma^i{}_{jk}$ , Riemann tensor  $R^i{}_{jkl}$ , Ricci tensor  $R_{ij}$ , Ricci scalar  $R$ , trace free Ricci tensor  $S_{ij}$  and Weyl tensor  $C_{ijkl}$ , with the indices  $\{i, j, k, l\}$  ranging from  $\{0, n - 1\}$ , where  $n$  is the number of

spacetime dimensions. Assuming convention, these are defined by:

$$\Gamma^i_{jk} = \frac{1}{2}g^{il}(\partial_j g_{lk} + \partial_k g_{lj} - \partial_l g_{jk}), \quad (1)$$

$$R^i_{jkl} = \partial_k \Gamma^i_{jl} - \partial_l \Gamma^i_{jk} + \Gamma^m_{jl} \Gamma^i_{mk} - \Gamma^m_{jk} \Gamma^i_{ml}, \quad (2)$$

$$R_{ij} = \partial_k \Gamma^k_{ij} - \partial_j \Gamma^k_{ik} + \Gamma^m_{ij} \Gamma^k_{mk} - \Gamma^m_{ik} \Gamma^k_{mj}, \quad (3)$$

$$R = g^{ij} R_{ij}, \quad (4)$$

$$S_{ij} = R_{ij} - \frac{R}{4} g_{ij}, \quad (5)$$

$$C_{ijkl} = R_{ijkl} + \frac{1}{2}(g_{il}R_{jk} + g_{jk}R_{il} - g_{ik}R_{jl} - g_{jl}R_{ik}) + \frac{1}{6}(g_{ik}g_{jl} - g_{il}g_{jk})R. \quad (6)$$

The indices may be raised and lowered respectively by applying the metric or the inverse metric,  $g^{ij}$ . Several invariants require the dual of the Weyl tensor:  $C^*_{ijkl} \equiv \frac{1}{2}\epsilon_{ijmn}C^{mn}_{kl}$  where  $\epsilon_{ijmn}$  is the Levi-Civita tensor density. The formalism to compute the tensors for thin-shell wormholes is outlined in [6]. Two copies of Minkowski flat space on either side of the wormhole's throat are assumed, identical regions from each space are removed, and then separate regions along the boundary are identified. This formalism leads to a well-behaved wormhole, with the throat being located at the identical boundary between the separate regions. In this formalism, the metric is modified to be:

$$g_{ij}(x) = \Theta(\eta(x))g^+_{ij}(x) + \Theta(-\eta(x))g^-_{ij}(x), \quad (7)$$

where  $g^\pm_{ij}$  is the metric on the respective sides,  $\Theta(\eta(x))$  is the Heaviside-step function and  $\eta(x)$  is the outward pointing normal from the wormhole's throat. The radius of the wormhole's throat is located at the point the regions overlap,  $x = a$  (that  $x \geq a$  is important to note in regards to analyzing divergences). This formalism requires the second fundamental form  $K_{\mu\nu}^\pm$  for the analysis at the throat:

$$K_{ij}^\pm = \pm \begin{pmatrix} 0 & 0 & 0 & 0 \\ 0 & \frac{1}{R_1} & 0 & 0 \\ 0 & 0 & \frac{1}{R_2} & 0 \\ 0 & 0 & 0 & 0 \end{pmatrix}, \quad (8)$$

where  $R_1$  and  $R_2$  are the radii of curvature of the wormhole on either side. The thin-shell formalism modifies the Riemann tensor to become:

$$R_{ijkl} = -\delta(\eta)[k_{ik}n_j n_l + k_{jl}n_i n_k - k_{il}n_j n_k - k_{jk}n_i n_l] + \Theta(\eta)R_{ijkl}^+ + \Theta(-\eta)R_{ijkl}^-. \quad (9)$$

where  $\delta(\eta)$  is the delta function,  $k_{ij} = K_{ij}^+ - K_{ij}^-$  is the discontinuity in the second fundamental form, and  $n_i$  is the unit normal to the shell. The fourteen different GD invariants

has been defined in [1, 8]. Listed below are the formulas for the GD invariants.

$$I_1 \equiv C_{ij}{}^{kl} C_{kl}{}^{ij}, \quad (10)$$

$$I_2 \equiv -C_{ij}{}^{kl} C^*{}_{kl}{}^{ij}, \quad (11)$$

$$I_3 \equiv C_{ij}{}^{kl} C_{kl}{}^{mn} C_{mn}{}^{ij}, \quad (12)$$

$$I_4 \equiv -C_{ij}{}^{kl} C^*{}_{kl}{}^{mn} C_{mn}{}^{ij}, \quad (13)$$

$$I_5 \equiv R, \quad (14)$$

$$I_6 \equiv S_i{}^j S_j{}^i, \quad (15)$$

$$I_7 \equiv S_i{}^j S_j{}^k S_k{}^i, \quad (16)$$

$$I_8 \equiv S_i{}^j S_j{}^k S_k{}^l S_l{}^i, \quad (17)$$

$$I_9 \equiv C_{ikl}{}^j S^{kl} S_j{}^i, \quad (18)$$

$$I_{10} \equiv -C^*{}_{ikl}{}^j S^{kl} S_j{}^i, \quad (19)$$

$$I_{11} \equiv (C_{ilm}{}^j C_{jno}{}^i + C^*{}_{ilm}{}^j C^*{}_{jno}{}^i) S^{lm} S^{no}, \quad (20)$$

$$I_{12} \equiv (C_{ilm}{}^j C^*{}_{jno}{}^i - C^*{}_{ilm}{}^j C_{jno}{}^i) S^{lm} S^{no}, \quad (21)$$

$$I_{13} \equiv (C_{ilm}{}^j C_{jno}{}^k + C^*{}_{ilm}{}^j C^*{}_{jno}{}^k) S^{lm} S^{no} S_k{}^i, \quad (22)$$

$$I_{14} \equiv (C_{ilm}{}^j C^*{}_{jno}{}^k - C^*{}_{ilm}{}^j C_{jno}{}^k) S^{lm} S^{no} S_k{}^i. \quad (23)$$

The full solutions to the wormhole metrics studied herein were found using Wolfram Mathematica<sup>®</sup> and are provided in Appendix B.

### 3 Thin-Shell Flat-Face Wormhole

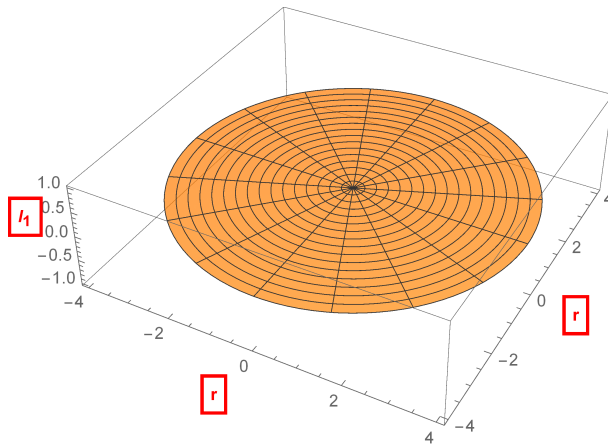


Figure 1: A plot of  $I_1$  for the TS wormhole. The plot is in radial coordinates with  $r \in \{0, 4\}$ . Notice that  $I_1$  is identically zero throughout the region. All other invariant functions that look identical to this figure are equal to zero.

The TS wormhole is one of the simplest wormhole solutions. It consists of two separate regions of Minkowski spacetime. A small portion of each region is sliced out. Their boundaries are identified as being the same to connect the two regions. To construct the wormhole, the radii,  $R_1$  and  $R_2$ , of curvatures in (8) were taken to  $\infty$  causing  $K_{ij}$  to vanish. The metric for the spacetime on either side of the throat is the Minkowski metric,

$$ds^2 = -dt^2 + dx^2 + dy^2 + dz^2. \quad (24)$$

By computing the thin shell formalism in Wolfram Mathematica<sup>®</sup>, the fourteen invariants were found and are recorded in (B.1). All the associated invariants vanish. A plot of  $I_1$  in Figure 1 is included to demonstrate the invariants' shape for flat space or identically zero curvature. The plot forms a single round disk with no divergences, singularities, discontinuities or other artifacts which might prevent travel through a TS wormhole.

## 4 Morris and Thorne Wormhole

The MT wormhole is defined by a spherically symmetric Lorentzian spacetime metric,  $ds^2$ , which describes the required traversable wormhole geometry. In the standard Schwarzschild coordinates [1], the metric is:

$$ds^2 = -e^{2\phi^\pm(r)} c^2 dt^2 + \frac{dr^2}{\left(1 - \frac{b^\pm(r)}{r}\right)} + r^2(d\theta^2 + \sin^2\theta d\varphi^2), \quad (25)$$

where the standard spherical coordinates are used ( $r$  : with circumference =  $2\pi r$ ;  $0 \leq \theta \leq \pi$ ;  $0 \leq \varphi \leq 2\pi$ ),  $t$  ( $-\infty < t < \infty$ ) is the proper time of a static observer,  $\phi^\pm(r)$  is the freely specifiable redshift function that defines the proper time lapse through the wormhole throat,  $b^\pm(r)$  is the freely specifiable shape function that defines the wormhole throat's spatial (hypersurface) geometry, and  $\pm$  indicates the side of the wormhole. The throat described by (25) is spherical. A fixed constant,  $r_0$ , is chosen to define the radius of the wormhole throat such that  $b^\pm(r_0) = r_0$ , which is an isolated minimum. Two coordinate patches of the manifold are then joined at  $r_0$ . Each patch represents either a different part of the same universe or another universe, and the patches range from  $r_0 \leq r < \infty$ . The use of Schwarzschild coordinates in (25) leads to more efficient computations of the Riemann and Ricci curvature tensors, the Ricci scalar, and all fourteen invariants.

Using Wolfram Mathematica<sup>®</sup>, all fourteen invariants were computed and are recorded in (B.2) through (B.8). All the invariants depend only on the radial coordinate,  $r$ , implying they are spherically symmetric. Eight of the invariants,  $I_2, I_4, I_9, I_{10}, I_{11}, I_{12}, I_{13}$ , and  $I_{14}$ , were zero with plots of these identical to Figure 1. Six of the invariants,  $I_1, I_3, I_5, I_6, I_7$ , and  $I_8$ , are non-zero. Upon inspection,  $I_1$  and  $I_3$  are linearly dependent as  $I_3 = \frac{I_1}{6r^3}$ . The Wronskian of  $I_1, I_5, I_6, I_7$ , and  $I_8$  was computed to check for linear independence and is non-zero making these invariants linearly independent.

The non-zero invariants are plotted in Figure 2 after selecting  $\Phi(r) = 0$  for the redshift and the shape function

$$b(r) = 2GM(1 - e^{r_0-r}) + r_0 e^{r_0-r}. \quad (26)$$

These functions satisfy the constraints required by [6] as discussed in Appendix A.2. At a distant greater than  $0.5r_0$ , all the figures are flat, which corresponds to zero curvature. For  $r \rightarrow 0$ , the figures for  $I_1, I_5, I_6$ , and  $I_8$  diverge to infinity. The divergence at  $r = 0$  is not pathological. As mentioned prior, the radial coordinate  $r$  has a minimum  $r_0 > 0$  at the wormhole's throat. Thus, a traveler passing through the wormhole would not experience any divergence. Any tidal forces on the traveler would be minimal. Consequently, the MT

wormhole would be traversable as indicated by the included invariant plots.

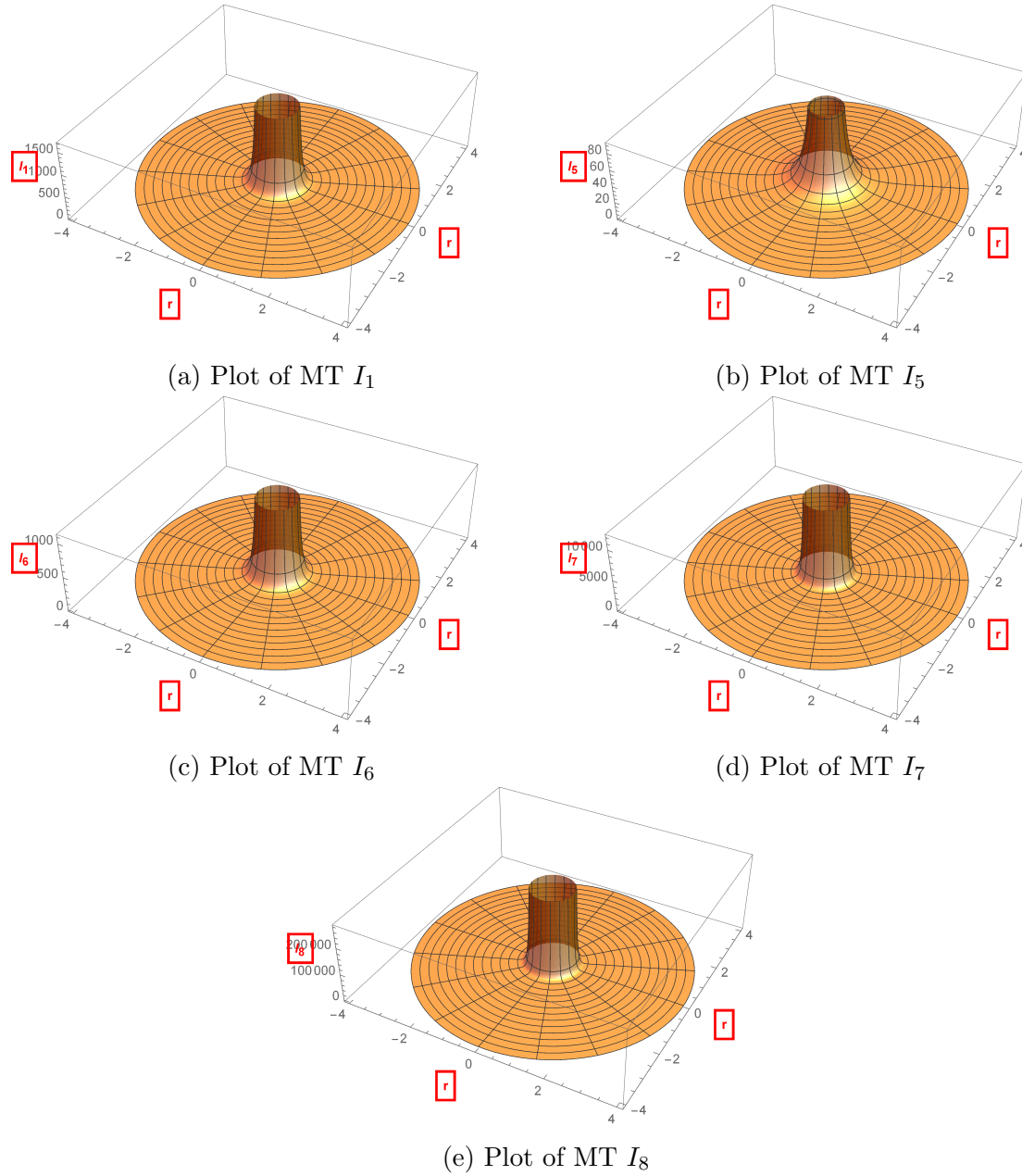


Figure 2: Plots of the non-zero invariants for the MT wormhole. The plots are in radial coordinates with  $r \in \{0, 4\}$ . Notice the divergence at the center of each plot is completely inside the  $r = 2 = r_0$  radial line. None affect the traversability of the wormhole.

## 5 Thin-Shell Schwarzschild Wormhole

A final example wormhole is the Schwarzschild wormhole. It is constructed by the steps described in [6]. The Schwarzschild geometry is given by the metric:

$$ds^2 = - \left(1 - \frac{2M}{r}\right) dt^2 + \frac{dr^2}{\left(1 - \frac{2M}{r}\right)} + r^2 (d\theta^2 + \sin^2\theta d\varphi^2), \quad (27)$$

where  $M$  is the mass of the wormhole. The standard spherical coordinates are used. The thin-shell formalism is applied with a unit normal  $n_i = \left(0, \sqrt{1 - \frac{2M}{r}}, 0, 0\right)$  in the notation of [7]. Regions described by  $\Omega_{1,2} \equiv \{r_{1,2} \leq a \mid a > 2M\}$  are removed from the two spacetimes leaving two separate and incomplete regions with boundaries given by the time-like hypersurfaces  $\partial\Omega_{1,2} \equiv \{r_{1,2} = a \mid a > 2M\}$ . The boundaries  $\partial\Omega_1 = \partial\Omega_2$  at the wormhole throat of  $r = a$  are identified and connected. The resulting spacetime manifold is geodesically complete and contains two asymptotically flat regions connected by the wormhole.

The fourteen curvature invariants were computed for the Schwarzschild wormhole using Wolfram Mathematica<sup>®</sup> and are recorded in (B.9) through (B.11). The mass and radius of the throat are normalized to  $M = 1$  and  $a = \frac{3}{2}$  as required by the Einstein equations and equation of state in [6]. All curvature invariants vanish with the exceptions of  $I_1$  and  $I_3$ . (Like the MT invariants the zero valued invariants appear identical to Figure 1.) The Wronskian of  $I_1$  and  $I_3$  are found to be non-zero, making the two linearly independent. The real portions of  $I_1$  and  $I_3$  are plotted in Figure 3.

The plots of  $I_1$  and  $I_3$  each have one divergence and a discontinuity. The divergence occurs at  $r = 0$ , which is outside the manifold of  $\Omega_{1,2}$ . By the same argument for the apparent MT divergence, the first Schwarzschild divergence would not impede the traversal of the wormhole. The discontinuity occurs at  $r = a = \frac{3M}{2}$ , which is located at the position where the horizons are connected by Schwarzschild wormholes. In these invariants, it is represented by a discontinuous jump from  $I_1(r) = I_3(r) = 0$  to

$$I_1(a) = \frac{64}{81M^4} - \frac{320}{2187M^2} - \frac{64 \csc^4 \theta^4}{2187M^2}, \quad (28)$$

and

$$I_3(a) = \frac{512}{729M^6}. \quad (29)$$

Since the invariants at the horizon are inversely proportional to  $M^2$ ,  $M^4$  and  $M^6$ , the tidal forces on a traveler is benign at the horizon.

A second discontinuity occurs in  $I_1$  at  $r = a$  and  $\theta = \{0, 2\pi\}$  due to the coordinate singularity in spherical polar coordinates that is not defined at this point in the manifold. It is represented by the empty patch at  $r = a$  and  $\theta = 0$  in Figure 3a. Interestingly,  $I_3$  contains both real and imaginary values proportional to  $(\delta(r - a))^3 \left(1 - \frac{2M}{a}\right)^{\frac{9}{2}}$ . Since  $a = \frac{3M}{2}$ , this term will be imaginary inside the horizon. While of interest, neither of these artifacts affect traversal of the wormhole.



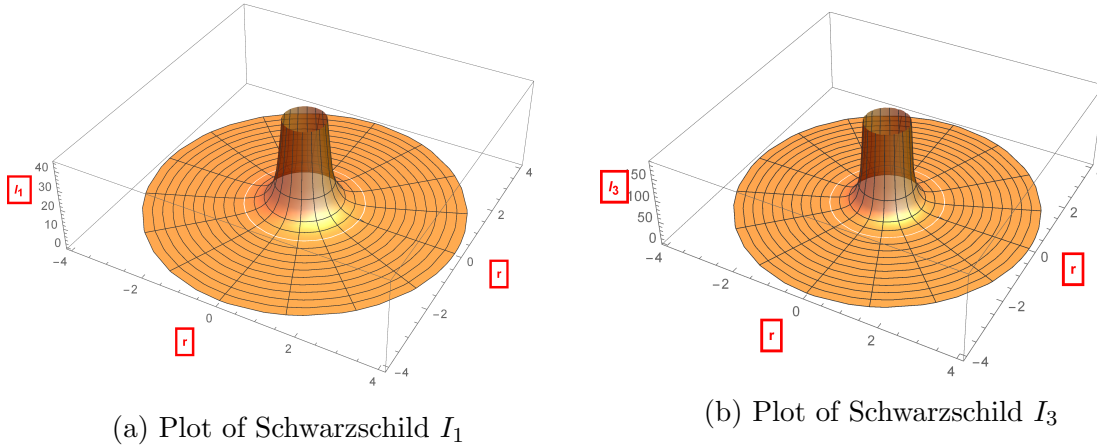


Figure 3: Plots of the non-zero invariants for the Schwarzschild wormhole. The plots are in radial coordinates with  $r \in \{0, 4\}$ . Notice the divergence at the center of each plot is completely inside the  $r = 2 = r_0$  radial line. Thus, it will not affect the traversability of the wormhole. In addition, notice the ring discontinuity at  $r = 2 = r_0$ . It results from the  $\delta$ -function in the thin-shell formalism.

## 6 Conclusion

This paper demonstrates how computing and plotting the curvature invariants of various wormholes can reveal whether the wormhole is traversable or not. As examples, it is indicated that *(i)* TS, *(ii)* spherically symmetric MT, and *(iii)* thin-shell Schwarzschild wormholes are traversable in agreement with [2, 3, 6]. The invariants of the TS wormhole are shown to be all zero and are plotted in Figure 1. It is shown that the only non-zero and independent invariants for the MT are  $I_1$ ,  $I_5$ ,  $I_6$ ,  $I_7$ , and  $I_8$ , which are plotted in Figures 2a-2e. A divergence is found in all five, but it does not affect the wormhole's traversability since the divergence is outside the physical range of the radial coordinate,  $r \in (r_0, \infty)$ . For the thin-shell Schwarzschild wormhole,  $I_1$  and  $I_3$  are found to be the only non-zero, independent invariants. As plotted in Figures 3a and 3b, these two have a divergence at the center and a ring discontinuity. The divergences are outside the physical radial coordinate and can be safely ignored. The ring discontinuity represents a jump due to the  $\delta$ -function from the thin-shell formalism. The ring discontinuity is shown to be inversely proportional to  $M^4$ , not affecting the traversal through the wormhole.

Potentially, the ring discontinuity could lead to a redshift of light rays passing through the wormhole. The redshift could be used to distinguish wormholes from black holes. While significant research remains to answer traversable wormhole issues, especially with regards to the mass requirements and understanding averaged null energy condition violations. The present paper hopes to establish several methods for understanding the traversal through wormholes.

Computing and plotting the invariant functions has significant advantages for the inspection of wormholes. As mentioned previously, the advantage of plotting the invariants is that they are free from coordinate mapping distortions and other artifacts of the chosen



coordinates. The resulting invariants properly illustrate the underlying spacetime revealing the presence of any artifacts, divergences or discontinuities, independent of coordinate system. Once the artifacts are revealed by the invariants, they can be related mathematically to the standard tensors. Their effect on a objects motion can then be analyzed. A second advantage is the relative ease with which the invariants can be plotted. Software packages exist or can be developed to calculate the standard tensors. The aforementioned tensors lead to a chosen basis of invariants. While the GD invariants were chosen to be computed and plotted in this paper, other choices of invariants exist, such as the Witten and Petrov. These can be computed and plotted without difficulty. Since the invariants are either scalars or pseudoscalars, they can be straightforwardly plotted and visually interpreted.

The form of the invariant functions and plots for other wormhole metrics can be hypothesized based on the three wormhole metrics studied in this paper. The TS wormhole chosen in this paper is the simplest of a large class of thin-shell wormholes which include spherical, cubic, and polyhedral types. While the second fundamental form is identically zero and leads to zero-valued invariants for the chosen TS metric, second fundamental forms for other thin-shell wormholes may not be identically zero, since they depend on the two radii of curvature,  $R_1$  and  $R_2$ , of the throats. As a consequence of the  $\delta$ -functions in the thin-shell formalism, these radii would likely lead to jump discontinuities in the general thin-shell invariants similar to those found in the thin-shell Schwarzschild wormhole. Another direction for thin-shell wormholes study is to investigate a more realistic metric on either side of the wormhole (such as the Friedmann metric). Another variation of thin-shell wormholes is to model different radii of curvature on either side of the wormhole. Thin-shell wormholes with unequal radii can be further extrapolated to wormholes with different times or universes on either side of the throat.

The thin-shell Schwarzschild wormhole is also the most common example of a large class of wormholes. The class includes wormholes with different radii of curvature and/or masses on either side of the throats, wormholes with same or different charge,  $Q$ , on either side of the wormhole, and time-dependent wormholes. For charged wormholes, a second ring artifact at  $r = Q$  is likely to exist since the metric has a singularity at that point.

A prospective future application of this work is an investigation of dynamic wormholes. Dynamic wormholes are the ones where the radii of the two throats change over time. This implies that the ring discontinuity in the invariant functions will change as a function of time. Hence, dynamic wormholes are technically more intricate to study as compared to static wormholes. Consequently, it can be expected that the computation of a dynamic wormhole's invariants and their plots increase in difficulty and runtime. In a broader perspective, the calculation and plotting of curvature invariants can be made to encompass other types of FTL travel such as the Alcubierre warp drive [12].

## 7 Acknowledgements

E. W. Davis would like to thank the Institute for Advanced Studies at Austin for supporting this work.

## A Appendices

### A.1 Riemann Curvature Invariants

Riemann curvature invariants are scalar products of the Riemann, Ricci, and Weyl tensors and their traces, covariant derivatives, and/or duals. Invariants are measures of curvature, which is defined as the amount upon which the space-time geometry differs from being flat [8]. The prime example of the invariants are scalar polynomial (SP) invariants such as the Kretschmann invariant,  $R^{ijkl}R_{ijkl}$ , though other types exist, such as the Cartan invariants. This paper focuses on the SP invariants (the SP prefix should be assumed). In the invariants, Einstein summation is performed over repeated indices, resulting in a scalar function formed from various polynomials. Reference [8] notes that the complete set of invariants are important in studying general relativity since they allow a manifestly coordinate invariant characterization of certain geometrical properties of spacetimes. Invariants are critical for studying curvature singularities, the Petrov type of the Weyl tensor and the Segre type of the trace free Ricci tensor, and for studying the equivalence problem\*. In this paper, the invariants are primarily used to study the curvature singularities.

A simple example of a sphere given in [9] can help illustrate the use of invariants. The metric of a 2-sphere is

$$g_{ij} = \begin{pmatrix} a^2 & 0 \\ 0 & a^2 \sin^2 \theta \end{pmatrix}. \quad (\text{A.1})$$

where  $a$  is the radius of the sphere. There are two nonzero components of the Riemann tensor,  $R^1_{221} = \sin^2 \theta$  and  $R^1_{212} = \sin^2 \theta$ , computed from (2), which fully determine the curvature of the sphere. However, normally we think of the curvature in terms of the Gaussian curvature computed from (4). For the sphere,  $R = \frac{1}{a^2}$ , which is related with the circle bounding the equator. Alternatively, any other invariant for other characteristics of the curvature can be computed. For example, the Kretschmann invariant gives  $R^{ijkl}R_{ijkl} = \frac{2}{a^4}$ , which can be connected with the surface area of the sphere. Here, the curvature invariants measure the curvature of the manifold and not the object's path through the manifold. Unfortunately, the invariants in Appendix B are not as simple as the invariants of the sphere. To gain a physical insight into the nature of the invariants, they must be plotted as is done herein.

---

\*The equivalence problem is whether two different metrics lead to identical spacetimes [8].

Riemann invariants are divided into three groups: the Weyl, the Ricci, and the mixed. In general, there are 4 independent Weyl invariants ( $I_1 - I_4$  in this paper) given by the real and complex parts of functions defined as  $I$  and  $J$  in [8]. As for the Ricci invariants, there are 4 independent real Ricci invariants ( $I_5 - I_8$  in this paper) formed of the Ricci scalar and three traces or covariant derivatives of the Riemann, Ricci, or trace-free Ricci tensors. There are at least 6 different mixed invariants ( $I_9 - I_{14}$  in this paper) formed by combining traces and covariant derivatives of combinations of the Riemann, Ricci, or trace-free Ricci tensors.

As discussed in [11], singularities come in three types in general relativity: coordinate, removable, and intrinsic. Coordinate singularities result from a coordinate system only covering a portion of the manifold. The classic example is Schwarzschild coordinates used in (25) and (26), which do not cover the axis at  $\theta = \{0, \pi\}$  because the line element becomes degenerate and the metric ceases to be of rank 4. Coordinate singularities are removable by a proper change of coordinates and will not appear in the invariants. As illustrated in Figures 3a and 3b, the coordinate singularity does not manifest itself in the plots as expected.

The removable type of singularity can be apparently seen in the metric, but vanishes in any calculated invariants. As an example, the singularity in the metric in (27) at  $r = 2M$  is removable. Upon inspection of the invariants in (B.10) and (B.11), the  $r = 2M$  singularity is removed by replacement with a  $\delta$ -function. In the Figures 3a and 3b, the singularity is absent.

The final type of singularity is an intrinsic (a.k.a. a curvature, physical, essential, or real) singularity. This type of singularity can not be removed by any proper change of coordinates and remains a singularity in the invariants. An example of an intrinsic singularity is the  $r = 0$  singularity seen in (B.3) - (B.8), (B.10), and (B.11). This can be seen in each of the plots: 2a - 2e, 3a, and 3b. However, it should be noted that an invariant blowing up at a point does not necessarily imply a singularity exists in the spacetime manifold. For example, this paper defined its coordinates in a way not to pass through the  $r = 0$  singularity in any of the spacetimes considered herein.

## A.2 The Morris and Thorne Redshift and Shape Functions

The MT Wormhole given in (25) has two freely specifiable functions i.e., the redshift function,  $\phi_{\pm}(r)$ , and the shape function,  $b_{\pm}(r)$ . These two functions satisfy the consistency requirements as [6] entails.

The redshift function must have:

1. continuity of the  $t$  coordinate across the throat,  $\phi_+(r_0) = \phi_-(r_0)$ ,
2. existence and finiteness of both the limits,  $\lim_{r \rightarrow \pm\infty} \phi(r) = \phi_{\pm}$ .

These two aforementioned constraints are the minimum required for a traversable wormhole. However, additional constraints can be imposed by choice on the redshift function for ease of calculations and temporal and spatial symmetry.

The shape function must have:

1. existence and finiteness of both the limits,  $\lim_{r \rightarrow \pm\infty} b(r) = b_{\pm}$ ,
2. the masses of the wormhole  $M_{\pm}$  on the two sides as given by  $b_{\pm} = 2GM_{\pm}$ ,
3.  $\exists r_* \parallel \forall r \in (r_0, r_*)$ ,  $b'(r) < \frac{b(r)}{r}$ ,
4.  $b_+(r_0) = b_-(r_0)$  and  $b'_+(r_0) = b'_-(r_0)$  at the throat.

The shape function chosen in (26),  $b(r) = 2GM(1 - e^{r_0-r}) + r_0e^{r_0-r}$ , obeys the listed conditions, with  $\lim_{r \rightarrow \pm\infty} b(r) = 2GM$ . Thus, the shape function at the throat exists, is finite, and is continuous, which satisfies the second and the fourth conditions. At the throat (i.e.,  $r \rightarrow r_0$ ),  $b(r) = r_0$ . The derivative,  $b'(r) = (2GM - r_0)e^{r_0-r} = b(r) + 2GM$ , is in agreement with the third condition mentioned above<sup>†</sup>.

The freely specified shape function can have a significant impact on the form of the invariant functions. By inspecting the invariants in Appendix B, it is seen that a shape function with a term of  $r^n$  with  $n \geq 3$  will not have a discontinuity at  $r = 0$ . For example, a shape function

$$b(r) = \frac{r^3}{r_0^3} (e^{r_0-r}), \quad (\text{A.2})$$

gives a plot of  $I_1$  in Figure 4. The discontinuity at  $r = 0$  has been replaced by an inverted cone with a finite depth. While this is outside the domain of  $r$  as discussed in §4, it demonstrates the effect that the shape function holds over the invariants.

---

<sup>†</sup>Since  $G > 0$  and  $M > 0$ ,  $b'(r) < \frac{b(r)}{r}$  for all  $r_0 \leq r \leq \infty$  instead of a specific range of  $r_*$  as necessitated by the third condition.

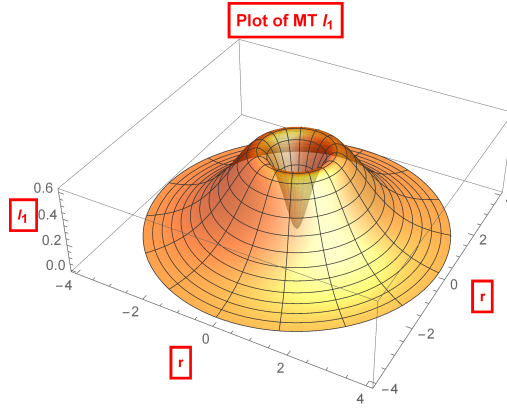


Figure 4: Plot of MT  $I_1$  for the shape function given in (A.2). The plots are in radial coordinates with  $r \in \{0, 4\}$ .

## B Invariants

### B.1 Invariants for the Thin Shell Wormhole

$$I_1 = I_2 = I_3 = I_4 = I_5 = I_6 = I_7 = I_8 = I_9 = I_{10} = I_{11} = I_{12} = I_{13} = I_{14} = 0. \quad (\text{B.1})$$

## B.2 Invariants for the Morris-Thorne Wormhole

$$I_2 = I_4 = I_9 = I_{10} = I_{11} = I_{12} = I_{13} = I_{14} = 0, \quad (\text{B.2})$$

$$I_1 = \frac{1}{3r^6} \left[ b(r)(2r^2\Phi''(r) + 2r^2\Phi'(r)^2 - 3r\Phi'(r) + 3) - r(b'(r)(1 - r\Phi'(r)), \right. \\ \left. + 2r(r\Phi''(r) + r\Phi'(r)^2 - \Phi'(r))) \right]^2, \quad (\text{B.3})$$

$$I_3 = \frac{1}{18r^9} \left[ b(r)(2r^2\Phi''(r) + 2r^2\Phi'(r)^2 - 3r\Phi'(r) + 3) - r(b'(r)(1 - r\Phi'(r)) \right. \\ \left. + 2r(r\Phi''(r) + r\Phi'(r)^2 - \Phi'(r))) \right]^3, \quad (\text{B.4})$$

$$I_5 = \frac{1}{r^2} \left[ (3b(r) - 4r)\Phi'(r) - 2r(r - b(r))\Phi'(r)^2 + b'(r)(2 + r\Phi'(r)) \right. \\ \left. + 2r(b(r) - r)\Phi''(r) \right], \quad (\text{B.5})$$

$$I_6 = \frac{1}{4r^6} \left[ b(r)^2(6 - 4r^3\Phi'(r)^3 + 4r^4\Phi'(r)^4 - 8r^2\Phi''(r) + 4r^4\Phi''(r)^2 \right. \\ - 4r\Phi'(r)(r^2\Phi''(r) - 3) + \Phi'(r)^2(r^2 + 8r^4\Phi''(r))) + r^2(b'(r)^2(2 + r^2\Phi'(r)^2) \\ - 4rb'(r)\Phi'(r)(r^2\Phi''(r) + r^2\Phi'(r)^2 - 2) + 4r^2(r^2\Phi'(r)^4 + r^2\Phi''(r)^2 \\ + 2\Phi'(r)^2(1 + r^2\Phi''(r))) - 2rb(r)(b'(r)(2 + r^2\Phi'(r)^2 - 2r^3\Phi'(r)^3 \\ + \Phi'(r)(6r - 2r^3\Phi''(r))) + 2r(2r^3\Phi'(r)^4 - r^2\Phi'(r)^3 + \Phi'(r)(2 - r^2\Phi''(r)) \\ \left. + 2r\Phi''(r)(r^2\Phi''(r) - 1) + 2\Phi'(r)^2(2r^3\Phi''(r) + r)) \right], \quad (\text{B.6})$$

$$I_7 = \frac{1}{8r^9} 3 \left[ b(r)(1 + 2r\Phi'(r)) - r(b'(r) + 2r\Phi'(r)) \right]^2 \left[ b(r)(2r^2\Phi''(r) + 2r^2\Phi'(r)^2 \right. \\ \left. - r\Phi'(r) - 2) + r^2(b'(r)\Phi'(r) - 2r(\Phi'(r)^2 + \Phi''(r))) \right], \quad (\text{B.7})$$

$$I_8 = \frac{1}{256r^{12}} \left[ r^4((3b(r) - 4r)\Phi'(r) - 2r(r - b(r))\Phi'(r)^2 + b'(r)(r\Phi'(r) - 2) \right. \\ + 2r(b(r) - r)\Phi''(r))^4 + 2(b(r)(2 + r\Phi'(r) - 2r^2\Phi'(r)^2 - 2r^2\Phi''(r)) \\ + r^2(2r(\Phi''(r) + \Phi'(r)^2) - b'(r)\Phi'(r)))^4 + (b(r)(2r^2\Phi''(r) + 2r^2\Phi'(r)^2 \\ \left. - 5r\Phi'(r) - 4) + r(b'(r)(r\Phi'(r) + 2) - 2r(r\Phi''(r) + r\Phi'(r)^2 - 2\Phi'(r))) \right)^4. \quad (\text{B.8})$$

### B.3 Invariants for the Thin Shell Schwarzschild Wormhole

$$I_2 = I_4 = I_5 = I_6 = I_7 = I_8 = I_9 = I_{10} = I_{11} = I_{12} = I_{13} = I_{14} = 0, \quad (\text{B.9})$$

$$I_1 = \frac{4}{r^4} + \frac{16M^2(a-2M)^3\delta(r-a)^2}{a^7} + \frac{16(a-2M)^3\csc^4(\theta)(r-2M)^2\delta(r-a)^2}{ar^6} + \frac{16(a-2M)^3(r-2M)^2\delta(r-a)^2}{ar^6}, \quad (\text{B.10})$$

$$I_3 = \frac{8}{r^6} - \frac{64M^3(a-2M)^4\sqrt{1-\frac{2M}{a}}\delta(r-a)^3}{a^{10}} - \frac{64\left(1-\frac{2M}{a}\right)^{9/2}\left(a-\frac{2aM}{r}\right)^3\delta(r-a)^3}{r^6} + \frac{64a^3\left(1-\frac{2M}{a}\right)^{9/2}(2M-r)^3\csc^6(\theta)\delta(r-a)^3}{r^9}. \quad (\text{B.11})$$



## References

- [1] Henry, R. C., Overduin, J. and Wilcomb K. (2016), “A New Way to See Inside Black Holes,” arXiv:1512.02762v2 [gr-qc].
- [2] Morris, M. S. and Thorne, K. S. (1988), “Wormholes in spacetime and their use for interstellar travel: A tool for teaching general relativity,” *Am. J. Phys.*, Vol. 56, pp. 395–412.
- [3] Morris, M. S., Thorne, K. S. and Yurtsever, U. (1988), “Wormholes, time machines, and the weak energy conditions,” *Phys. Rev. Lett.*, Vol. 61, pp. 1446 – 1449.
- [4] Ellis, H. G. (1973), “Ether flow through a drainhole: A particle model in general relativity,” *J. Math. Phys.*, Vol. 14, pp. 104 – 118.
- [5] Bronnikov, K. A. (1973), “Scalar-tensor theory and scalar charge,” *Acta Physica Polonica*, Vol. B4, pp. 251 – 266.
- [6] Visser, M. (1995), *Lorentzian Wormholes: From Einstein to Hawking* (New York: AIP Press).
- [7] Christoffel, E. B. (1869), “Ueber die Transformation der homogenen Differentialausdrücke zweiten Grades,” *Journal für die reine und angewandte Mathematik*, Vol. 70, pp. 46 – 70.
- [8] Zakhary, E. and McIntosh, C. B. G. (1997), “A Complete Set of Riemann Invariants,” *Gen. Relativ. Gravit.*, Vol. 29, pp. 539 – 581.
- [9] MacCallum, M. A. H. (2015), “Spacetime invariants and their uses,” arXiv:1504.06857v1 [gr-qc].
- [10] Henry, R. C. (2000), “Kretshmann Scalar for a Kerr-Newman Black Hole,” *The Astrophysical Journal*, Vol. 535, pp. 350 – 353.
- [11] D’Inverno, R. C. (1992), *Introducing Einstein’s Relativity* (Oxford: University Press)
- [12] Alcubierre, M. (1994), “The warp drive: hyper-fast travel within general relativity,” *Class. Quant. Grav.*, Vol. 11, No. 5, pp. L73-L77.